

# Ultrahigh-Current-Density Tribovoltaic Nanogenerators Based on Hydrogen Bond-Activated Flexible Organic Semiconductor Textiles

Guoxu Liu, Beibei Fan, Youchao Qi, Kai Han, Jie Cao, Xianpeng Fu, Zhaozheng Wang, Tianzhao Bu, Jianhua Zeng, Sicheng Dong, Likun Gong, Zhong Lin Wang, and Chi Zhang\*



Cite This: *ACS Nano* 2025, 19, 6771–6783



Read Online

ACCESS |



Metrics & More

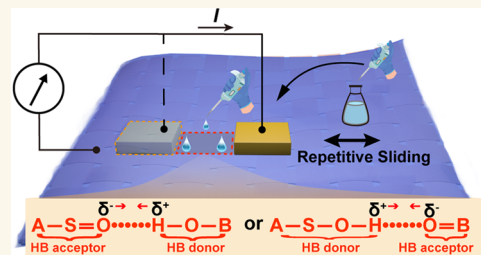


Article Recommendations



Supporting Information

**ABSTRACT:** The polymer-based triboelectric nanogenerator (TENG) has long grappled with the constraint of limited current density (CD), whereas semiconductor-based triboelectric nanogenerators, using the tribovoltaic effect, have shown promising potential for achieving high current density. This study introduces an effective solution—a direct current tribovoltaic nanogenerator with ultrahigh current density—founded on a flexible organic semiconductor textile activated by solvents. By introducing 95% ethyl alcohol, an ultrahigh current density of 8.75 A/m<sup>2</sup> and peak power density of 1.07 W/m<sup>2</sup> are demonstrated, marking a striking enhancement of 438-fold and 170-fold, respectively, in comparison to the friction surface without 95% ethyl alcohol. The activation mechanism is that the poly(vinyl alcohol) dissolution by solvents exposes more PEDOT:PSS, and the formation of hydrogen bonds with PSS<sup>−</sup> releases more active PEDOT<sup>+</sup>. This advancement finds practical utility, as evidenced by successful demonstrations involving cell phone charging and small motor propulsion. The breakthrough unveiled in this work presents vistas for the widespread application of flexible organic semiconductor textile-based tribovoltaic nanogenerators, offering exciting opportunities for biomechanical energy harvesting.



**KEYWORDS:** tribovoltaic nanogenerators, high current density, EA activation, organic semiconductor, textile-based

## INTRODUCTION

Biokinetic energy acquisition plays a pivotal role in powering self-sustained portable electronic devices and sensors within the Internet of Things (IoT) ecosystem.<sup>1,2</sup> While conventional energy storage units such as batteries or capacitors face limitations in providing consistent power, the emergence of renewable, abundant, and sustainable biokinetic energy presents an opportunity to develop lightweight, flexible, and high-performance energy harvesters.<sup>3–5</sup> More impressively, the year 2012 marked a significant milestone with the introduction of the triboelectric nanogenerator (TENG), an innovative energy acquisition approach.<sup>6</sup> Functioning on the principles of contact electrification and electrostatic induction, the TENG relies on the second term of Maxwell's displacement current for its theoretical foundation.<sup>7,8</sup> Compared to traditional energy collection methods such as electromagnetism, photovoltaic, and thermoelectric, TENGs offer distinct advantages, including their lightweight nature,<sup>9,10</sup> miniaturization,<sup>11,12</sup> low cost,<sup>13,14</sup> and high energy conversion efficiency.<sup>15–17</sup> These

attributes position TENGs as a promising solution for biokinetic energy harvesting.

In recent years, researchers have discovered that when the surfaces of a p-type semiconductor and an n-type semiconductor slide against each other, direct current (DC) flows between the two electrodes at the top of the p-type semiconductor and the bottom of the n-type semiconductor, a phenomenon known as the tribovoltaic effect.<sup>18–20</sup> The mechanism is that the energy released by the new chemical bonds formed at the interface by mechanical sliding creates electron–hole pairs at the PN junction and the internal electric field formed at the PN junction separates the electrons from the holes, resulting in a DC output. The energy released by the

**Received:** August 11, 2024  
**Revised:** January 31, 2025  
**Accepted:** January 31, 2025  
**Published:** February 12, 2025



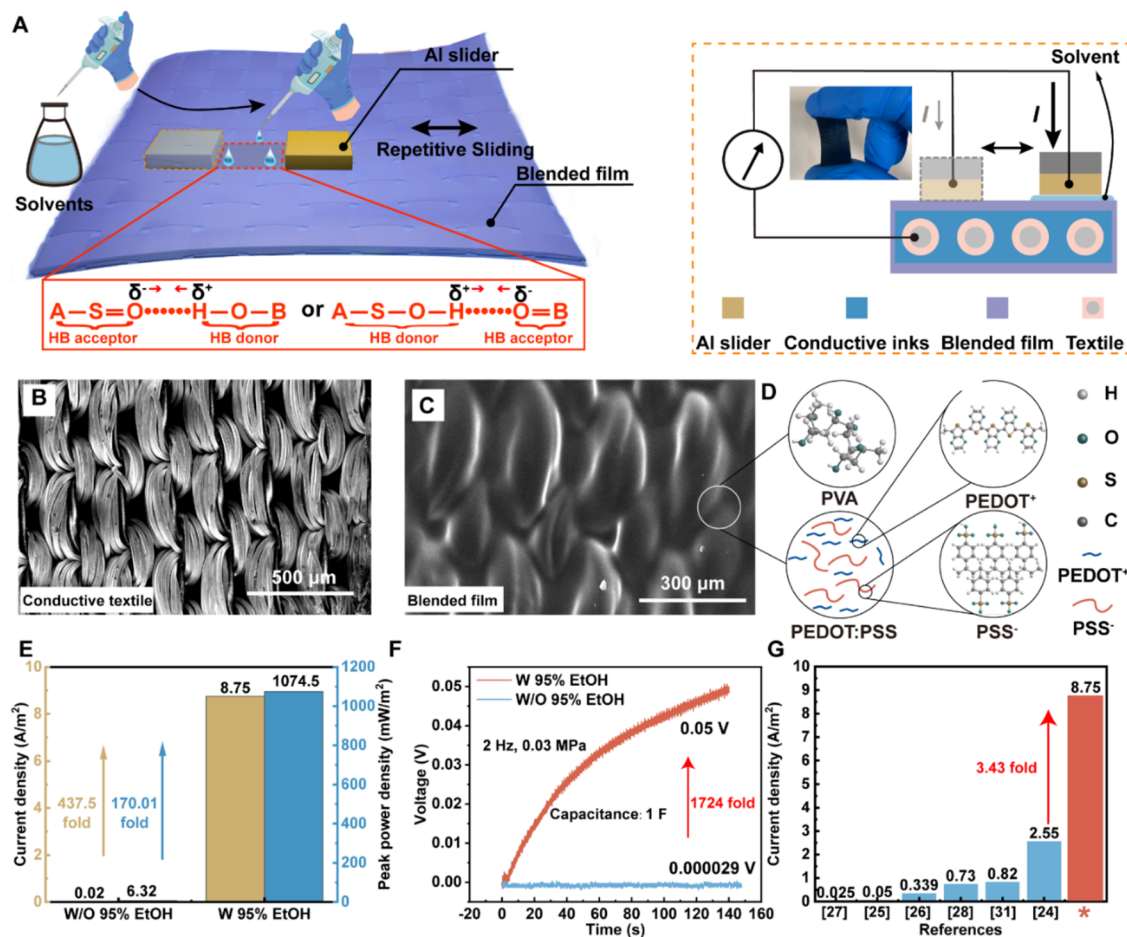


**Figure 1.** Basic structure and constituents of flexible organic textile tribovoltaic generators (FO-TTG). (A) 3D schematic diagram of the flexible organic textile tribovoltaic generator (FO-TTG). The FO-TTG is composed of several layers: a hydrophobic conductive textile, hydrophilic conductive ink, a blended film (BF) consisting of 88.89 wt % poly(vinyl alcohol) (PVA) and 11.11 wt % poly(3,4-ethylenedioxythiophene): poly(styrenesulfonate) (PEDOT:PSS is abbreviated as P:P), and an Al slider. Solvent drops at the interface between the friction materials form HBs, releasing more of the active ingredient PEDOT<sup>+</sup>. The cross-sectional view of the film highlights the multilayer structure of FO-TTG, with an inset photo showing a bent BF. (B, C) Scanning electron microscopy (SEM) image of the surface appearance of the bare conductive textile and the BF. (D) Molecular structures involved in the blended film. It showcases the long-chain structure of P:P and the long-chain molecular structures of PVA, PEDOT<sup>+</sup> molecular structures (positively charged PEDOT), and PSS<sup>-</sup> molecular structures (negatively charged poly(styrenesulfonate)). (E) Graphs comparing the current density (CD) and peak power density (PPD) of FO-TTG before and after dropping 95% EtOH. CD and PPD were enhanced by 438- and 170-fold, respectively. (F) Graph comparing the charging efficiency of a 1 F capacitor between FO-TTG (2 cm × 2 m) with and without dripping 95% EtOH on the friction interface. The 95% EtOH activation leads to a significant increase in charging efficiency. (G) Graph comparing the CD of FO-TTG with previously reported works. The CD of FO-TTG is significantly higher than that of organic- or inorganic-based DC TVNG. The CD at the centimeter level in this study is approximately 3.43-fold higher than that of previously reported inorganic TVNG.

formation of chemical bonds is known as a “bondington”, which is an exciton that excites the electron–hole pair, like the photovoltaic effect.<sup>21,22</sup> Tribovoltaic nanogenerator (TVNG) is prepared using this mechanism of operation and are characterized by low internal resistance (IR) (~kΩ) and high current density (CD) (~A/m<sup>2</sup>).<sup>23,24</sup> However, the hard material characteristics of inorganic semiconductors severely limit the wide application of DC TVNG.<sup>25–29</sup> Overcoming the limitations of inorganic semiconductors, researchers have explored organic semiconductor-based DC TVNGs, combining similar output characteristics with flexibility, stretchability, and ease of fabrication.<sup>30–34</sup> Key contributions in this field include Shao et al.’s work on a metal–organic semiconductor device, generating an open-circuit voltage ( $V_{OC}$ ) of 0.25 V and a short-circuit CD of 0.339 A/m<sup>2</sup>.<sup>26</sup> Additionally, Meng et al.’s research introduced an organic flexible textile DC nano-

generator achieving an output CD of 0.025 A/m<sup>2</sup> through the tribovoltaic effect.<sup>27</sup> The author’s previous work introduced PEDOT:PSS (P:P) organic semiconductor-based DC TVNGs with outputs reaching 0.73 A/m<sup>2</sup> and 0.8 V on a centimeter scale.<sup>33</sup> Such advancements hold promise for next-generation wearable energy harvesting devices. Nonetheless, further improvements are necessary to meet the power requirements of self-powered electronic devices.

This article introduces an effective approach: flexible organic textile tribovoltaic nanogenerators (FO-TTG) activated by hydrogen bonds (HBs) formation. Compared to nonactivated performance, the introduction of 95% Ethyl alcohol (EtOH) on the friction interface leads to an astonishingly high CD of 8.75 A/m<sup>2</sup> and a peak power density (PPD) of 1074.5 mW/m<sup>2</sup>, marking enhancements of 438- and 170-fold, respectively, in comparison to the friction surface without 95% Ethyl

alcohol. More impressively, this achievement showcases a CD over 3.43-fold greater than previously reported inorganic-based TVNG with the maximum CD. The active mechanism involving solvents lies in its ability to screen the ionic interaction between PEDOT<sup>+</sup> and PSS<sup>-</sup> by forming HBs with PSS<sup>-</sup>. The activation mechanism is that the poly(vinyl alcohol) (PVA) dissolution by solvents exposes more PEDOT:PSS, and the formation of hydrogen bonds with PSS<sup>-</sup> releases more active PEDOT<sup>+</sup>. This breakthrough sets a new CD record for TENGs with the potential to revolutionize flexible organic semiconductor textile-based TVNGs, particularly for biokinetic energy harvesting applications.

## RESULTS AND DISCUSSION

**Structure and Basic Constituents of FO-TTG.** Textile-based kinetic energy harvesting devices represent a promising avenue for providing continuous power to portable electronic devices. In this context, we propose the development of FO-TTG, an effective biokinetic energy harvesting device composed of a blended film (BF) containing 11.11 wt % P:P and 88.89 wt % PVA. As illustrated in Figure 1A, the 3D configuration of FO-TTG shows its fundamental composition, encompassing a hydrophobic conductive textile (CT), a hydrophilic conductive ink layer, a BF layer, and an Al film slider. (The manufacturing process and materials are detailed in the Materials and Methods section). The arrangement facilitates the collection of mechanical energy through actions such as reciprocating sliding friction, which is then converted into DC electricity. Notably, the textile coated with conductive ink and the BF offers flexibility, deformation capability, and commendable skin conformability (inset photo in Figure 1A). Introducing solvents onto the friction interface significantly amplifies the output CD of the FO-TTG, a phenomenon whose underlying mechanisms will be discussed in detail below.

P:P, a conductive organic polymer, PEDOT<sup>+</sup> acts as its primary semiconductor component, while PSS<sup>-</sup> acts as a dispersant, enhancing the water solubility of P:P. With PVA also exhibiting high water solubility, aqueous solutions of PVA and P:P seamlessly blend into a homogeneous solution. The conductive textile, composed of nylon fibers interwoven with silver thread, possesses a hydrophobic nature, characterized by gaps and small openings (Figures 1B and S1A). To mitigate the surface energy of the textile and minimize the presence of residual air bubbles during the coating process, an initial layer of hydrophilic conductive ink is applied to the conductive textile (Figure 1C, bottom left of Figure S1B and Notes S1 and S2). The scanning electron microscopy (SEM) image in the bottom right of Figure S1B offers insight into the multilayer cross-sectional structure of the BF, depicting the snug coverage of the flexible conductive textiles by the conductive ink and BF. After a 4-h drying period, the surface characteristics of the BF are illustrated in Figure S1C. Additionally, Figure S2 presents X-ray diffraction (XRD) patterns of blended P:P films with varying doping concentrations, revealing a crystalline peak at  $2\theta = 19.4^\circ$ , attributed to the (1, 0, -1) crystal plane, a hallmark of PVA. Conversely, bare P:P films lack such crystalline reflections. Thermogravimetric analysis, and derivative thermogravimetric analysis conducted on bare PVA films, bare P:P films, and BFs highlight two distinct phases in the BF (Figure S3 and Note S3).

The blending of P:P with PVA introduces a break in the continuity of the original P:P macromolecular chain, resulting

in a significantly reduced surface conductivity of the BFs in comparison to the bare P:P film.<sup>33</sup> This disruption in surface conductivity translates to output characteristics characterized by low current and elevated internal resistance (IR) when the Al slider repetitively slides the surface of the BF. The molecular architecture of P:P entails PEDOT<sup>+</sup> molecules linked to PSS<sup>-</sup> through ionic bonds, as demonstrated in the inset of Figure 1D, which also showcases the 3D molecular models of long-chain PVA, PEDOT<sup>+</sup>, and PSS<sup>-</sup>. Detailed molecular structures of all solvents and solutes employed in this study can be found in Figure S4, including PVA, dichloromethane (DCM), dimethyl sulfoxide (DMSO), EtOH, ethylene glycol (EG), water, PEDOT<sup>+</sup>, and PSS<sup>-</sup>. More impressively, the incorporation of 95% EtOH on the friction interface substantially enhances the charging capacity of the FO-TTG for capacitors with significant magnitude. In Figure 1E, without any solvent introduction, the CD and PPD are only 0.02 A/m<sup>2</sup> and 6.32 mW/m<sup>2</sup>. With the introduction of 95% EtOH as the active solvent, the CD and PPD increased to 8.72 A/m<sup>2</sup> and 1074.5 mW/m<sup>2</sup>, respectively, which were enhanced by 438 and 170 times, respectively. The CD now obtained in this article exceeds all previously reported centimeter-scale TVNGs, both organic-based and inorganic-based, and is a 3.43 times advancement in the record for existing TVNGs. The charging ability of FO-TTG for large capacitors was also characterized after introducing 95% EtOH (Figure 1F). The voltage across a 1 F capacitor reaches only 0.000029 V after 140 s of charging under 2 Hz and 30 kPa conditions. In stark contrast, under identical operating conditions, the introduction of 95% EtOH results in the capacitor voltage reaching 0.05 V, reflecting an impressive 1724-fold enhancement in voltage and a 2.97-million-fold increase in electrical energy. According to the data presented in Figure S5, the measured PPD of 1074.6 mW/m<sup>2</sup> exceeds that of previously reported organic semiconductor-based DC TVNGs at the centimeter level. Furthermore, as depicted in Figure 1G, the CD of 8.75 A/m<sup>2</sup> achieved in the work surpasses that of reported organic- or inorganic-semiconductor-based TVNGs at the centimeter scale.

**Output Performances of FO-TTG.** To comprehensively illustrate the output performance of the solvent-activated FO-TTG, a series of experiments were meticulously conducted. These experiments aimed to shed light on the behavior of the FO-TTG under continuous friction, which was simulated using a linear motor. Monitoring the force applied along the Z-axis, in conjunction with a force gauge, the experiments were further facilitated by the controlled drip of solvents, which was fully managed through a syringe pump and syringe. Detailed experimental parameters can be found in Figure S6 and Note S4. As illustrated in Figure S7, an array of BF samples with different P:P concentrations (ranging from 0 to 100 wt %) were prepared to explore the effect of these concentrations on output. When the Al slider slides back and forth directly on the BF, the output  $V_{OC}$  and CD are obviously related to the concentration of P:P. More impressively, a discernible correlation emerged: as the P:P concentration increased, the maximum  $V_{OC}$  (2.4 V, Figure S8A) and CD (0.04 A/m<sup>2</sup>, Figure S8B) were established. This correlation underscores the role of doped PVA in disrupting the formation of a P:P conductive network, which consequently hampers carrier transport and heightens surface resistance. Strikingly, the introduction of 95% EtOH onto the friction interface led to a remarkable surge in CD to approximately 10 A/m<sup>2</sup>—an astounding increase of approximately 1000-fold (Figure S8D).

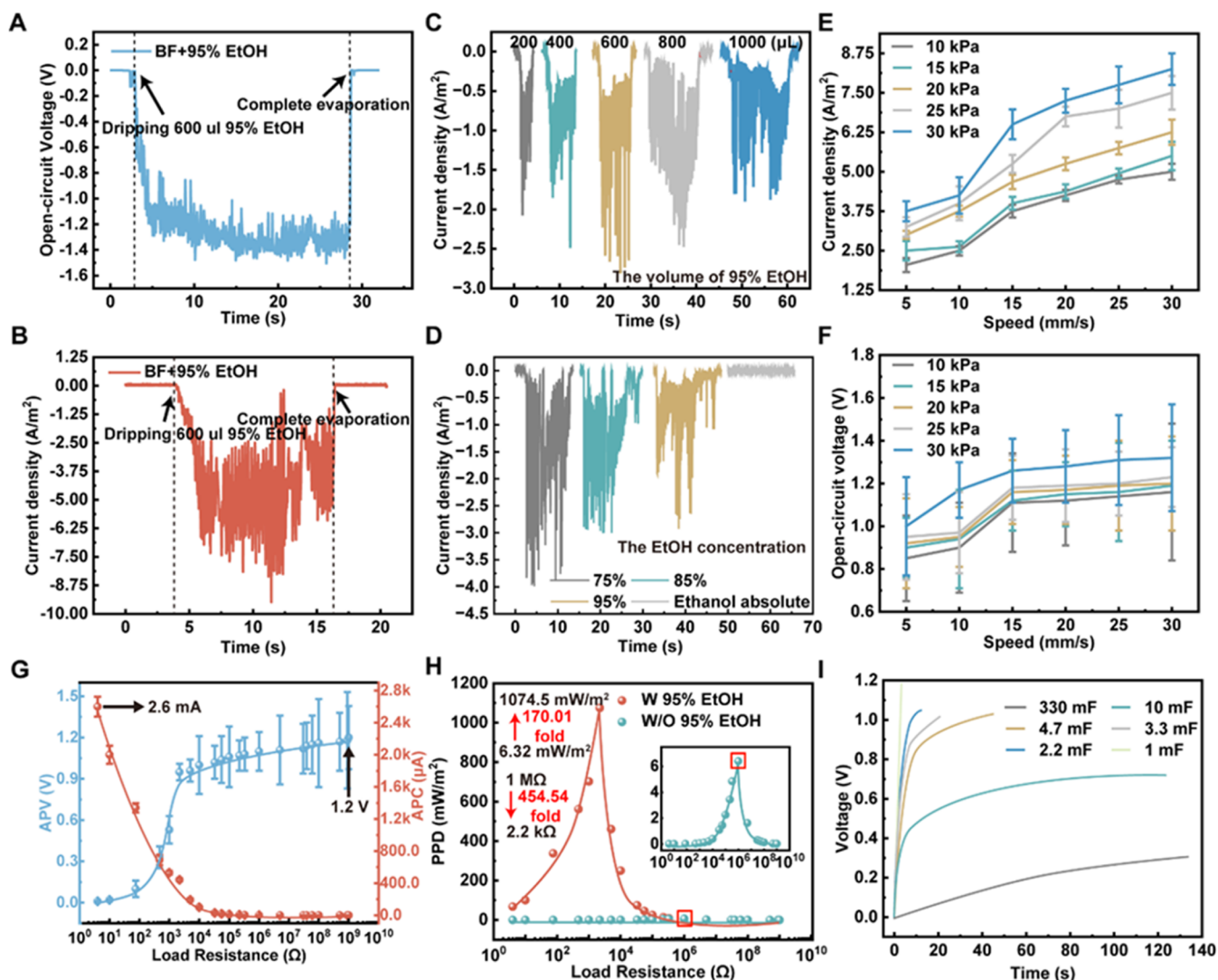


Figure 2. Output performance of FO-TTG (2 cm × 2 cm). With dripping 600  $\mu\text{L}$  of 95% EtOH on the friction interface, the output wave characteristics of (A) open-circuit voltage ( $V_{\text{OC}}$ ) and (B) CD. (C) Graph showing the change in the typical output CD of FO-TTG after dripping different volumes of 95% EtOH on the friction interface between the Al slider and the BF. (D) Plot demonstrating the variation in the output CD of FO-TTG when different concentrations of EtOH are dripped on the friction surface. The output CD is affected by the concentration of the EtOH solution. (E, F) Two subgraphs illustrating the positive correlation between the CD and  $V_{\text{OC}}$  of the FO-TTG and the increased sliding speed as well as the applied pressure intensity. The sliding speed ranges from 5 to 30 mm/s, and the pressure intensity ranges from 0.01 to 0.03 MPa. (G) Graph presenting the variation in the output average peak voltage (APV) and average peak current (APC) of FO-TTG with increasing load resistance. This response is observed after dripping 95% EtOH on the friction surface. (H) Variation of the PPD and internal resistance (IR) of the FO-TTG as the external resistance in parallel connection increases. The inset displays the PPD of FO-TTG without EtOH activation on the friction interface. (I) Comparison of the charging efficiency of the FO-TTG for different capacitors (ranging from 1 to 330 mF).

However, it is worth noting that the  $V_{\text{OC}}$  exhibited a marginal decline (1.2 V, Figure S8C). Given these outcomes, the BF composition of 11.11 wt % P:P and 88.89 wt % PVA emerged as the optimal choice for subsequent experiments. This blend consistently showed an equilibrium between favorable output performance and mechanical properties<sup>33</sup> (Figure S18). Hence, this composition was adopted in all ensuing experiments unless otherwise specified.

When the Al slider was subjected to repeated rubbing on the BF while receiving a 600  $\mu\text{L}$  drip of 95% EtOH on the friction surface, the detailed waveforms of  $V_{\text{OC}}$  and CD are unveiled in Figure 2A,2B. Further investigation into the effect of different volumes of EtOH was conducted on the output CD of FO-TTG, as depicted in Figure 2C. Notably, an interesting trend

emerged: with the dripping volume of 95% EtOH ranging from 200 to 1000  $\mu\text{L}$  on a 2 cm × 2 cm area, the CD initially rose and then declined, peaking at 600  $\mu\text{L}$ . This pattern of increase and subsequent decrease can be attributed to spraying large volumes of 95% EtOH leading to increased dissolution of PVA and disrupting the integrity of the BF. Similarly, when various concentrations of EtOH, including 75, 85, 95% EtOH, and ethanol absolute, were dropped onto the friction surface, the CD exhibited a clear downward trend (as seen in Figure 2D). This phenomenon can be attributed to higher concentrations of EtOH containing less water, thus leading to decreased dissolution of PVA and, subsequently, reduced release of the active ingredient PEDOT+.

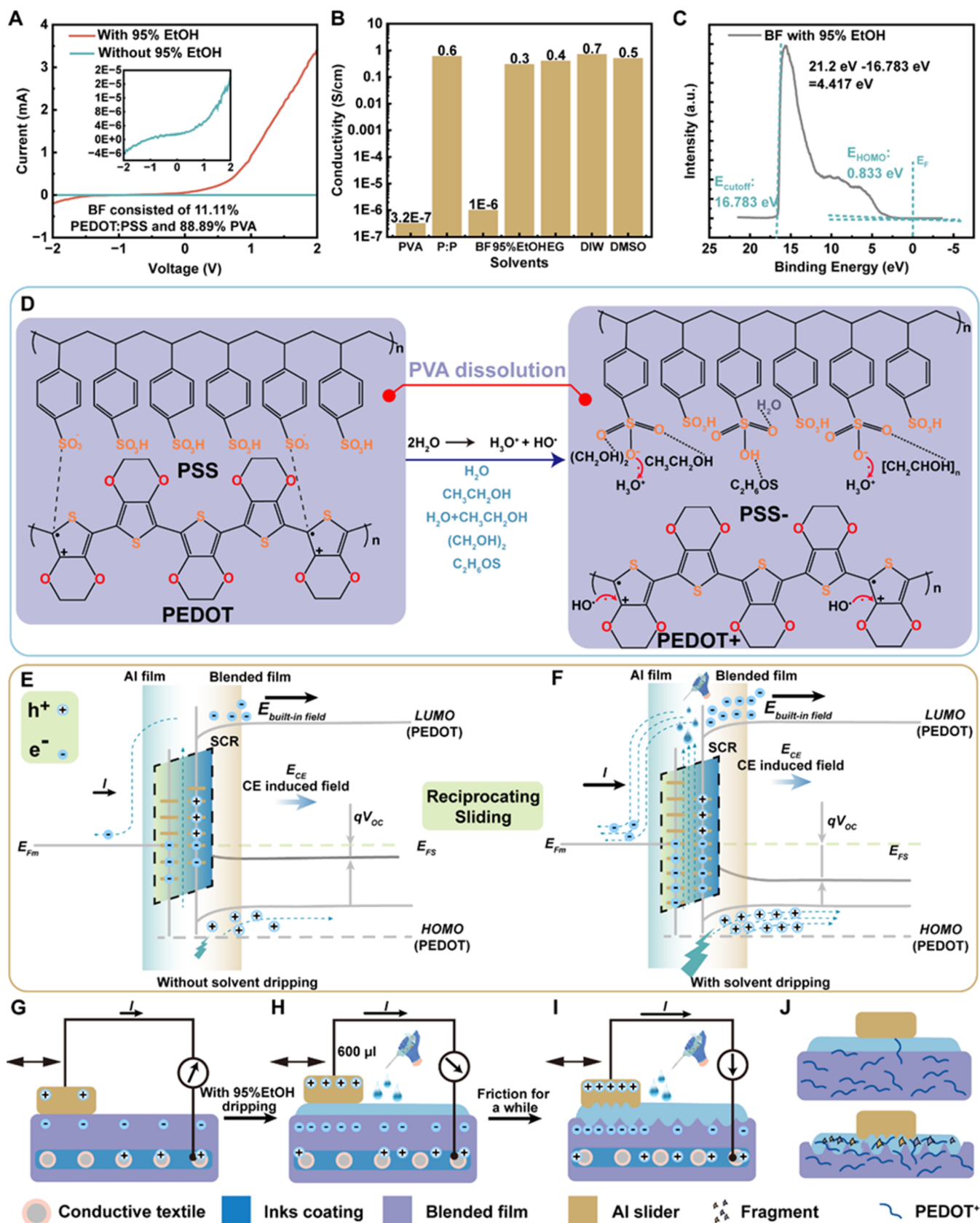


Figure 3. Working mechanism of the designed FO-TTG. (A) Graph comparing the current–voltage ( $I$ – $V$ ) curves of the BF and the Al slider with and without dripping of 95% EtOH. This illustrates the changes in current behavior under different conditions, demonstrating the impact of EtOH activation on the  $I$ – $V$  characteristics. (B) Plot showcasing the variation in conductivity of the BF when different solvents are dripped on the friction surface. The response of the BF conductivity to different solvents is depicted. (C) Ultraviolet photoelectron spectroscopy (UPS) spectra of a BF with 95% EtOH dripping. This provides insight into the electronic structure and energy levels of the

Figure 3. continued

material after EtOH activation. (D) Schematic illustration depicting the mechanism of ionic interaction between PEDOT<sup>+</sup> and PSS<sup>-</sup> in the absence of solvent dripping, while solvent dripping on the friction interface leads to the formation of HBs between solvent, water, or PVA molecules and SO<sub>3</sub><sup>-</sup> or SO<sub>3</sub>H of PSS<sup>-</sup>, resulting in the release of more PEDOT<sup>+</sup>. Schematic diagrams are presented to depict the energy band structures of FO-TTG without EtOH dripping on the friction interface. (E) Enhanced output with 95% EtOH dripping. (F) The change in energy levels and charge distribution is highlighted. (G) Schematic illustration showing the output current between the BF and the Al slider at the friction interface without the dripping of 95% EtOH. This demonstrates the low current output in this scenario. (H) By dripping 600  $\mu$ L of 95% EtOH on the friction interface, the output current is significantly increased. This is illustrated in a schematic diagram. (I) After a period of friction, the output current further increases due to the falling and dissolving of some PVA fragments. This leads to more contact between PEDOT<sup>+</sup> and the Al slider. (J) Comparison of the change in local surface morphology after initial friction and friction for a period is shown. After repeated friction, more PEDOT<sup>+</sup> contacts the Al slider, resulting in a further increase in the output current. This figure visually explains the working mechanism of the designed FO-TTG and how different factors contribute to its enhanced performance and output characteristics.

It is noteworthy that ambient temperature played a pivotal role in EtOH evaporation. Figure S9 illustrates the relationship between the 95% EtOH evaporation time and average short-circuit current ( $I_{SC}$ ) across varying ambient temperatures from 15 to 35 °C. Elevated temperatures resulted in accelerated solvent evaporation, which, counterintuitively, led to diminished FO-TTG output performance. This seemingly paradoxical outcome can be attributed to the prolonged interaction between the solvent and the friction interface. The extended contact facilitated greater dissolution of PVA and subsequent release of the active ingredient PEDOT<sup>+</sup>. To evaluate FO-TTG durability, a 1000 s test was performed at a 2 Hz frequency, as depicted schematically in Figure S10. Throughout the test, the  $V_{OC}$  maintained stability at 1.2 V (Figure S10A), while the CD exhibited a declining trajectory due to the continuous accumulation of Al and PVA fragments at the friction interface, consequently compromising frictional contact. Upon cleaning the friction surface,  $I_{SC}$  returned to its maximum value (Figure S10B). Continuous friction induced a gradual decrease in the BF thickness. Monitoring this evolution, glass was chosen as the substrate to allow precise measurement using a profile scanner at 5 min intervals. The outcome demonstrated a consistent decrease in film thickness with increasing friction time (Figure S10C). This thickness inhomogeneity variation stemmed from fluctuations in Z-axis pressure, contributing to inconsistencies in measured thickness cycle by cycle (Note S5). In the continuous friction process, SEM images of the BF surface were taken after 5000 cycles, 10,000 cycles, and 15,000 cycles, as shown in Figure 10D–F, respectively.

When subjected to different pressures and friction speeds, the peak value variations of CD and  $V_{OC}$  were summarized (Figure 2E,F). More impressively, both CD and  $V_{OC}$  exhibited positive correlations with the sliding speed (ranging from 5 to 30 mm/s) and pressure intensity (10–30 kPa). Direct sliding of the Al film on the BF yielded a  $V_{OC}$  and  $I_{SC}$  of approximately 2.34 V and 16  $\mu$ A, respectively (Figure S12A). Variations in load resistance, however, led to divergent outcomes: the average peak voltage (APV) displayed a descending trend, while the average peak current (APC) showed an opposite trajectory. Calculated by the product of current squared and resistance ( $I^2 \times R$ ), the PPD reached its zenith at 6.32 mW/m<sup>2</sup> with a 1 M $\Omega$  load resistance (Figure S12B).

In comparison, FO-TTG composed of a bare P:P film exhibited a PPD of 0.76 mW/m<sup>2</sup> under a 33 k $\Omega$  load resistance (Figure S12C,D). Upon introduction of 95% EtOH (600  $\mu$ L) to the friction interface, the APV slightly decreased ( $\sim$ 1.2 V), whereas the maximum APC surged dramatically ( $\sim$ 2.6

milliampere (mA); Figure 2G). Consequently, the PPD increased to 1074.5 mW/m<sup>2</sup> with a 2.2 k $\Omega$  load resistance. This outcome signifies not only a substantial 454.54-fold decrease in IR (from 1 M $\Omega$  to 2.2 k $\Omega$ ) but also an impressive 170.01-fold surge in output PPD (from 6.32 to 1074.5 mW/m<sup>2</sup>) (Figure 2H). Interestingly, the solvent activation extends beyond 95% EtOH, encompassing other solvents such as DMSO, DIW, and EG. The effects of these solvents on  $V_{OC}$  and CD are detailed in Figure S13A,B. Dripping DIW and DMSO on the friction surface, as revealed by the swelling ratio experiment, results in severe damage to the film integrity (Notes S6 and S7 and Figures S14–S17). In a mere 20 min immersion, the film samples dissolved entirely in DIW and DMSO. Additionally, EG droplets cause film shrinkage and distortion. In contrast, ethanol absolute has very little solubility and minimal impact on the BF. Incorporating a small volume of DIW into ethanol absolute not only enhances FO-TTG's output performance but also maintains the film's mechanical integrity (Figure S18 and Note S8). Upon considering these factors, the optimal choice is to employ a 95% volume ratio of EtOH. Further insights are available in Table S1 and Note S9. The changes in PPD and IR of FO-TTG when using different solvents are calculated and depicted in Figure S19, where PPD surpasses 300 mW/m<sup>2</sup> and IR reduces to the level of a few k $\Omega$ . All computed PPD and IR values for FO-TTG are summarized in Figure S20. Notably, the activation effect of 95% EtOH is substantially superior to those of other solvents. Moreover, the addition of 95% EtOH does not compromise the structural integrity of the BF and preserves its mechanical wear resistance. Consequently, the ensuing discussion of the enhancement mechanism is anchored in the context of using 95% EtOH for activation. A comparison of the charging efficiency of the FO-TTG for different capacitors (ranging from 1 to 330 mF) is provided in Figure 2I. The energy storage efficiency of a 1 mF capacitor is unimaginable for both conventional TENGs and previously reported TVNGs, as it can be charged from 0 to 1.2 V in just 2 s.

**The Working Mechanism of FO-TTG.** Illustrated in Figure 3 are the operational framework and cycle of the devised FO-TTG when activated by solvents. To comprehensively elucidate the mechanism triggered by 95% EtOH for the output current, current–voltage ( $I$ – $V$ ) curves of Al-bared P:P film-conductive textile (Al–P:P-CT) and Al-BF-conductive textile (Al-BF-CT) were measured, as exhibited in Figure S21. Both Al–P:P-CT and Al-BF-CT manifest rectification behavior indicative of Schottky contact.<sup>35</sup> The presence of a certain amount of PVA noticeably reduced the current level. The  $I$ – $V$  curve after 95% EtOH dripped on the friction

interface is displayed in Figure 3A, maintaining the rectification behavior associated with the Schottky contact. The forward bias voltage leads to an exponential increase in current, while the reverse bias voltage dependence remains weak. It is noteworthy that upon the application of a forward bias voltage of 2 V, the current reverts to the milliampere (mA) level due to the influence of 95% EtOH. The logarithmic  $I$ - $V$  characteristics of Al-P:P-CT, Al-BF-CT, and Al-BF-CT with 95% EtOH activation are shown in Figure S22A-C.

Analysis of the electrical properties of the Schottky contact can be undertaken through the thermionic emission theory, yielding the following expressions<sup>35</sup>

$$J = A^*T^2 \exp\left(-\frac{q\Phi_{ps}}{kT}\right) \left[ \exp\left(\frac{eV}{kT}\right) \right] \quad (1)$$

$$I_0 = AA^*T^2 \exp\left(-\frac{q\Phi_{ps}}{kT}\right) \quad (2)$$

In this equation,  $J$  represents the CD and  $I_0$  represents the saturation current, with its value being determined at  $V = 0$  V. The saturation current for the three FO-TTGs is calculated as  $1.45 \times 10^{-8}$ ,  $1.55 \times 10^{-9}$  and  $5.66 \times 10^{-5}$  A, respectively.  $A$  denotes the Schottky junction contact area ( $200 \mu\text{m} \times 200 \mu\text{m}$ ),  $A^*$  is the Richardson constant ( $32 \text{ A/cm}^2 \text{ K}^2$ ),  $T$  corresponds to the ambient temperature during testing ( $27^\circ\text{C}$ ),  $K$  signifies the Boltzmann constant,  $q$  symbolizes the electron charge, and  $\Phi_{ps}$  refers to the barrier height. From eq 2, the barrier height  $\Phi_{ps}$  is determined by

$$\Phi_{ps} = \frac{kT}{q} \ln\left(\frac{AA^*T^2}{I_0}\right) \quad (3)$$

Subsequently, using eq 3, the calculated barrier height emerges as  $\sim 0.65$  eV for Al-P:P-CT,  $\sim 0.71$  eV for Al-BF-CT, and  $\sim 0.43$  eV for Al-BF-CT with 95% EtOH activation.<sup>36-40</sup> This variation in barrier height is attributed to the organic interlayer altering the effective barrier height. Precisely, the physical barrier provided by PVA prevents direct contact between P:P and metal Al. Consequently, the work function (WF) of Al and the electron affinity of P/P undergo substantial shifts, thus leading to an elevation in barrier height. The reduction in the barrier height of the BF post-95% EtOH dripping on the friction interface stems from HBs formation among EtOH, water, or PVA molecules and PSS<sup>-</sup>, allowing for the release of more active ingredient PEDOT<sup>+</sup>.<sup>41</sup>

Earlier experimental results highlight the substantial impact of both PVA doping in P:P and 95% EtOH dripping at the friction interface on FO-TTG IR (Figure S20).<sup>34</sup> This is primarily attributed to the alteration of surface conductivity. The summarized characterization outcomes are depicted in Figure 3B. The surface conductivity of the bare P:P film was approximately 0.6 S/cm, which significantly decreases with increasing PVA doping concentration. In contrast, the surface conductivity of BF plummets to  $1 \times 10^{-6}$  S/cm. Activation by solvents on the BF surface, on the one hand, dissolves PVA to eliminate the physical spacing between the conductive component PEDOT<sup>+</sup> and, on the other hand, facilitates the formation of HBs between solvent molecules, water molecules, or PVA and PSS<sup>-</sup>, resulting in more PEDOT<sup>+</sup> release. To further expound on the alteration in barrier height resulting from PVA doping and solvents, the variation in the work function (WF) of different films is investigated. Ultraviolet

photoelectron spectroscopy (UPS) spectra of a 95% EtOH-activated BF, as well as UPS spectra of a bare P:P film and BF, are shown in Figures 3C and S23A,B. Recognizing metal Al's work function as 4.28 eV, the WF of the P:P employed here is determined to be  $\sim 4.767$  eV via UPS spectra (Note S10). Meanwhile, the WF of the BF is  $\sim 4.417$  eV. Regardless of whether it is the bare P/P film or the BF with or without 95% EtOH activation, holes are the predominant carriers. Within the P/P molecular chain, the active component is PEDOT<sup>+</sup>, while PSS<sup>-</sup> enhances water solubility. Figure 3D presents one of the components, PSS<sup>-</sup>, partially deprotonated with a negative charge, while the other component, PEDOT<sup>+</sup>, is a positively charged conjugated polymer built on polythiophene, leading to the binding of the two ionomers via ionic bonds.

Upon solvents (water, EtOH, EG) dripping on the BF surface, PVA dissolution encourages more exposed P:P, leading to HBs (O-H-O) formation between the O-H bonds in EtOH molecules, EG molecules, water molecules, PVA molecules, and S=O of SO<sub>3</sub><sup>-</sup> or SO<sub>3</sub>H in PSS<sup>-</sup>. When DMSO drips on the BF surface, the S=O bonds in DMSO will form HBs (O...H...O) with the O...H bonds of SO<sub>3</sub>H in PSS<sup>-</sup>. The free H<sub>3</sub>O<sup>+</sup> in aqueous solution approaches the PSS<sup>-</sup> group, while OH<sup>-</sup> moves toward the PEDOT<sup>+</sup> molecular chain. This disrupts the Coulombic interaction between PEDOT<sup>+</sup> and PSS<sup>-</sup>, releasing more PEDOT<sup>+</sup>. Molecular dynamics (MD) results also corroborate this phenomenon, as specific solvents (DMSO, EtOH, water, or EG) preferentially form HBs with SO<sub>3</sub><sup>-</sup> or SO<sub>3</sub>H, as discussed further in Note S11 and Figures S24-S29. This mechanism is also corroborated by the results of attenuated total reflection Fourier transform infrared spectroscopy characterization of BFs with different solvents added dropwise to their surfaces (Figure S30). The detailed argumentation process is in Note S12. Table S2 summarizes the enhancement mechanism and swelling ratio under various solvent dripping, illustrating the variation in activation mechanisms across different solvents.

In a state of equilibrium, the working mechanism of FO-TTG is shown in Figure S31, and a detailed discussion is presented in Note S13. When the Al slider is rubbed back and forth on the BF, a new disequilibrium is established at the friction interface, and the dual mechanisms of the  $E_{CE}$  and the  $E_{\text{built-in field}}$  jointly promote the directional movement of charge carriers. Over the course of repeated sliding, nonequilibrium carriers are excited within the thin space charge region (SCR) by absorbing friction energy (Figure 3E). Concurrently,  $E_{CE}$  renders the Al contact interface positively charged, while the BF surface assumes a negative charge. This is corroborated by the change in BF surface potential during repeated rubbing, as observed in a comparative experiment where the surface potential of the bare P:P film tends toward neutrality (Figure S32). In both mechanisms, the electric field direction is from the metal to the BF. The nonequilibrium carrier excitation results in a potential energy difference ( $qV_{OC}$ ), translating into a decrease in the Fermi level within the energy band diagram. This energy difference propels electrons to flow within the external circuit to perform electrical work (Figure 3G), elucidating the marginal increase in CD from  $\sim 0.0069$  to  $\sim 0.0387 \text{ A/m}^2$  (Figure S8B). Given PVA's enveloping of the conductive textile and active ingredient PEDOT<sup>+</sup>, the surface conductivity is substantially reduced ( $\sim 6$  to  $\sim 1 \times 10^{-6} \text{ S/cm}$ ), and the potential barrier height increases ( $\sim 0.65$  to  $\sim 0.71$  eV). Consequently, the surface electrons of the BF face challenges

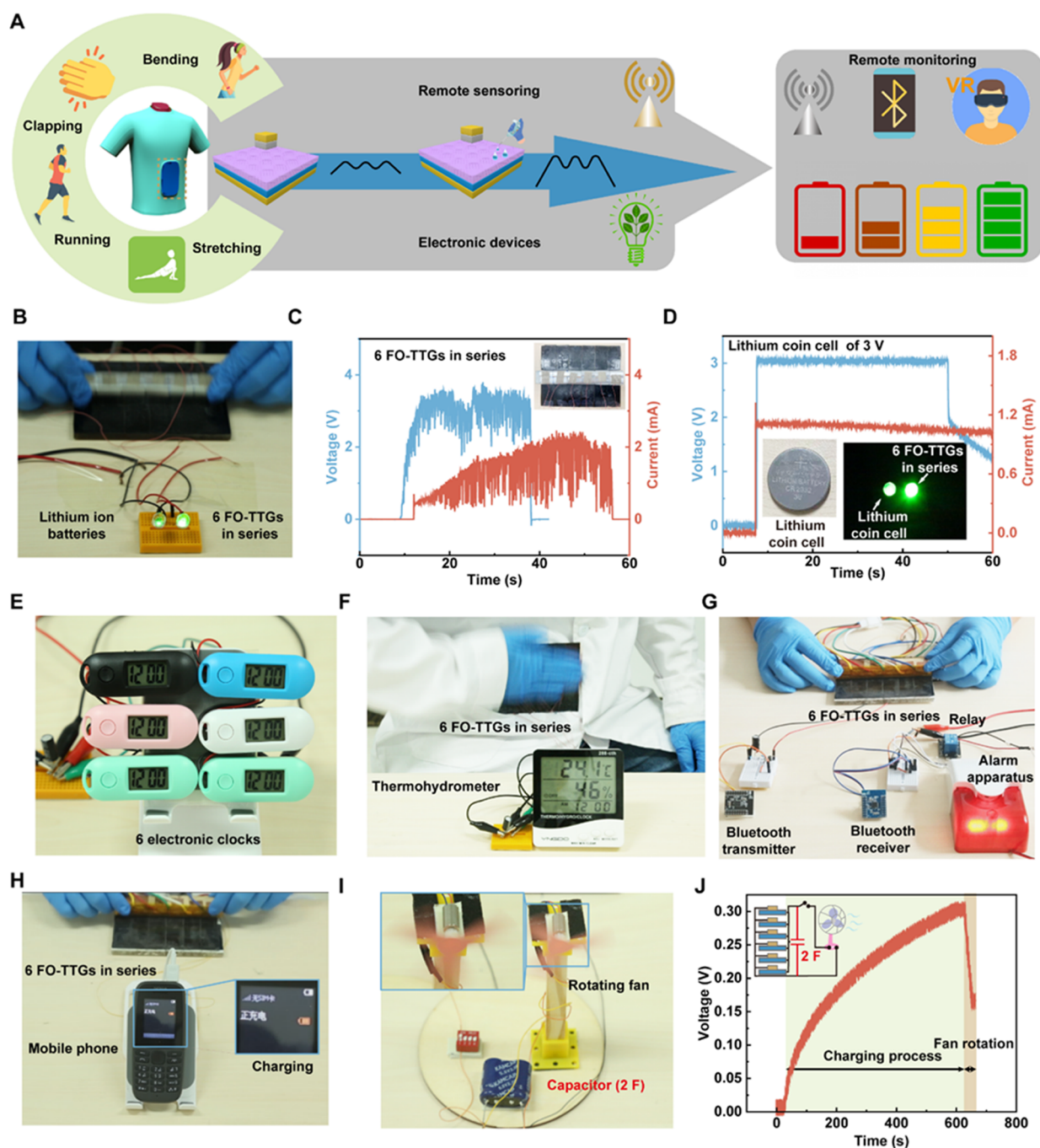


**Figure 4.** Application demonstration of 6 FO-TTGs in series or parallel. (A) Potential applications of FO-TTGs for remote sensing and self-powered electronics. (B) Comparison between 6 series-connected FO-TTGs and a commercial 3 V lithium coin cell used to drive LED. (C) Graph presenting the output voltage and current when an LED is driven by 6 FO-TTGs in series. (D) Output voltage and current when the LED is driven by a commercial lithium coin cell. (E) In the series state, with dripping EtOH on the friction interface, the short-circuit current reached approximately 1.7 mA, and the  $V_{OC}$  reached approximately 6.4 V. In the absence of power management, it completely meets the functional requirements of most low-power portable electronic devices. The 6 FO-TTGs in series simultaneously drive 6 electronic clocks in parallel. (F) When parallel connected with a 1 mF capacitor, the thermohydrometer is driven and continues working for 44 s, demonstrating the energy conversion capabilities of FO-TTGs. (G) Schematic diagram showing the setup of a commercial Bluetooth launch system driven by 6 FO-TTGs in series. This demonstrates how FO-TTGs can power wireless communication systems. (H) After EtOH drips and friction starts, the mobile phone displays a charging prompt information interface, indicating that it is being charged by the FO-TTGs. This figure provides practical demonstrations of the FO-TTGs' capabilities in driving various electronic devices and systems, emphasizing their potential for real-world applications in self-powered electronics and energy harvesting. (I) A small pink fan attached to a motor is driven by 6 FO-TTGs in parallel, showcasing their ability to power even small mechanical devices. (J) Graph illustrating the voltage variation of a 2 F capacitor, highlighting the energy transfer and utilization. The inset circuit connection diagram of 6 FO-TTGs in parallel drives a small motor.

traversing the external circuit promptly, significantly elevating the output  $V_{OC}$  average peak value ( $\sim 0.6$  to  $\sim 2.5$  V).

Upon introduction of 600  $\mu\text{L}$  of 95% EtOH by dripping on the friction interface, a small amount of PVA dissolves into DIW, facilitating the emergence of more active ingredient PEDOT+. The diffusion of energetic electrons at the Schottky interface in the Al slider to lower energy levels within PEDOT+, combined with several electrons transitioning to the lowest unoccupied molecular orbital (LUMO) energy level upon absorbing friction energy, leads to electron drift in opposition to the  $E_{\text{built-in field}}$  and  $E_{CE}$ . Simultaneously, induced holes migrate following the direction of the  $E_{\text{built-in field}}$  and  $E_{CE}$ , culminating in a more substantial current (Figure 3F). Additionally, the surface state change on the friction interface causes a fraction of electrons to leap to higher energy levels via the tunneling effect after absorbing friction energy, further facilitating carrier movement. The dripping of 95% EtOH on the friction interface diminishes the potential barrier ( $\sim 0.71$  to  $\sim 0.43$  eV), amplifying the quantity of nonequilibrium carriers to absorb increased friction energy and undergo transition. The depressed Fermi level of PEDOT+ establishes the  $qV_{OC}$  spurring electrons to traverse the external circuit (Figure 3H). The surface XPS spectra of the BF, bare P:P film, and bare PVA film following dropwise addition of EtOH and DIW validate the surface state change (Figure S33). Consequently, the dissolution of PVA and the change in the surface state collectively contribute to the increase in the output current.

In the course of reciprocating friction, fragments of the BF gradually detach and PVA fragments dissolve into 95% EtOH, thus releasing additional PEDOT+ (Figure 3J). This further enhances FO-TTG's output current (Figure 3I). The clarification that PEDOT+ release through PVA dissolution augments FO-TTG's output performance is presented in Figure S34 for FO-TTGs composed of a bare P:P film or BF with diverse solvents applied dropwise at the friction interface. Additional insights are provided in Note S14. Metals with different work functions are rubbed as friction layers against the blended films, and the output current densities are all enhanced, in agreement with the above analysis (Figure S35A–C). XRD patterns on the surface of the Al film before and after friction indicate that no chemical reaction occurs in this process (Figure S35D).

**Application Demonstrations of FO-TTG.** The primary objective of enhancing the output performance of flexible textile-based biokinetic energy harvesters is to achieve practical applications for sustainable rechargeable electronics and self-powered remote sensors. Traditional TENGs exhibit high  $V_{OC}$  and small  $I_{SC}$  due to their high IR. However, without an efficient power management strategy, they struggle to directly power low-consumption electronic devices at optimal energy conversion efficiency. In the case of a single FO-TTG (2 cm  $\times$  2 cm) under reciprocating friction (2 Hz, 30 kPa), the IR decreases to 2.2 k $\Omega$ , resulting in a relatively low  $V_{OC}$  of  $\sim 1.2$  V but an ultrahigh  $I_{SC}$  of  $\sim 2.5$  mA. By simply connecting multiple FO-TTGs in series or parallel, it is possible to directly power electronic devices using a coin cell or a single 1.5 V battery. Prior to the application demonstration, the  $V_{OC}$  and  $I_{SC}$  of six FO-TTGs in series or parallel connection configurations are measured. Under the series connection, one FO-TTG's Al slider is connected to another FO-TTG's conductive textile (Figure S36A). The  $V_{OC}$  and SCC will not immediately reach their peak values but rather do so within a few seconds (Figure S36B,C). This setup yields a pulse  $I_{SC}$  of

2.3 mA and a stable  $V_{OC}$  of 6.2 V, making it suitable for powering various low-power electronic devices and sensors. In the parallel configuration, the Al sliders and conductive textiles of six FO-TTGs are connected sequentially (Figure S36D). This arrangement results in a peak output  $I_{SC}$  of  $\sim 5.2$  mA, while the  $V_{OC}$  remains at  $\sim 2.3$  V (Figure S36E,F), which is not sufficient to power conventional portable electronic devices. Photos of six FO-TTGs in series (A) and in parallel (B) are shown in Figure S37. Each Al slider area measures 2 cm  $\times$  2 cm, and the BF area is 2 cm  $\times$  10 cm. Due to the micro protrusions and pits present on the surface of both the BF and the Al slider, the actual contact area of the friction material is smaller than the specified area.

The envisioned future application scenario for this energy collector involves harnessing various biokinetic energies to enable self-powered electronics and sensors (Figure 4A). Through 95% EtOH dripping onto the friction materials' interface, the output PPD and current experience significant enhancement. A visual comparison of six FO-TTGs connected in series and a commercial 3 V lithium coin cell powering an LED bulb is provided in Figure 4B. When the Al slider slides across the BF surface at 3 Hz, the average output of six series-connected FO-TTGs driving an LED reaches 3.3 V and 2.1 mA (Figure 4C), comparable to the brightness of an LED bulb driven by a 3 V lithium-ion battery (3 V, 1.1 mA) (Figure 4D and Movie S1). Given FO-TTG's unprecedented output current capacity, it is possible to simultaneously power six electronic clocks using biokinetic energy (Figure 4E and Movie S2). The circuit connection diagram for this application demonstration is illustrated in Figure S38A,B. Portable electronics, often with higher power consumption, require the connection of a parallel capacitor for energy storage, providing a stable power output through switch control. For instance, a thermohydrometer can detect the temperature and humidity while displaying the time. To demonstrate the stable operation of such portable electronics driven by FO-TTGs, six series-connected FO-TTGs connect a 1 mF capacitor in parallel and charge it for only 7 s using biokinetic energy, allowing the thermohydrometer to operate continuously for 44 s (Figure 4F and Movie S3).

As a demonstration of a self-powered wireless sensor driven by FO-TTGs, friction energy collected by a FO-TTG drives a Bluetooth transmitter to transmit a signal. The Bluetooth receiver triggers an alarm upon receiving the signal (Figure 4G). The voltage variation of a 1 mF capacitor during continuous Bluetooth signal emission is depicted in Figure S39A. Following capacitor voltage charging to 3 V, the Bluetooth transmitter successfully transmits a signal, prompting the alarm to send an alert signal. After EtOH is dripped on the friction interface again, the transmitter transmits the signal again (Movie S4). The circuit schematic diagram of the commercial Bluetooth transmitter and receiver is shown in Figure S39B, while component photos of the Bluetooth transmitter and receiver are listed in Figure S39C. Periodic battery charging of portable mobile phones is a common concern for users. In this research, when six series-connected FO-TTGs are activated by EtOH, the output is sufficient to charge a portable mobile phone (Battery parameter: BL-5CB, Capacity: 850 mAh) (Figure S40A,B). The circuit connection diagram for mobile phone charging is depicted in Figure S40C. Upon dripping EtOH and initiating friction, the mobile phone promptly displayed charging prompt information (Figure 4H and Movie S5), verifying its successful charging.

To further highlight FO-TTG's potent charging ability, an unprecedented application demonstration involving driving a micromotor is undertaken. The small pink fan attached to the motor clearly demonstrates its rotational state (Figures 4I and S41B,C). Six parallel-connected FO-TTGs first charge a 2 F capacitor to 0.3 V and then activate a switch, causing the small pink fan to operate for nearly 20 s (Movie S6). The variation in capacitor voltage during the charging and fan rotation processes is presented in Figure 4J. During the micromotor's operation, the instantaneous turn-on current is approximately 20 mA, a level of energy storage capacity that traditional TENGs cannot achieve (Figure S41A). The circuit connection diagram for driving a micromotor with six parallel-connected FO-TTGs is shown in the inset of Figure 4I.

## CONCLUSIONS

In summary, this study presents the development of an FO-TTG using the organic semiconductor P:P, achieving ultrahigh CD and PPD. The authors conduct a systematic investigation and characterization of the output characteristics of FO-TTG before and after the application of solvent on the friction interface. Through the activation of 95% EtOH on the friction interface, FO-TTG demonstrates a remarkable maximum CD of 8.75 A/m<sup>2</sup>, which is approximately 438-fold higher than that of the friction interface without any solvent dripping. The PPD reaches 1074.5 mW/m<sup>2</sup>, exhibiting an enhancement of approximately 170-fold compared to that of FO-TTG without solvent activation. This centimeter-level CD is approximately 3.43-fold higher than the existing TVNG's maximum CD in record, and the measured PPD is approximately 1.6-fold higher than that of previously reported organic TVNG. The experimental results reveal that FO-TTG's ability to charge a large capacitance is remarkably exceptional due to its robust current output capacity. Upon further analysis of the experimental findings, it is suggested that the enhancement mechanism is attributed to the solubilization of PVA by solvents, which contributes to the release of more P/P. Additionally, the formation of HBs between the solvent molecules or PVA molecules and PSS<sup>-</sup> screens the ionic interaction between PEDOT<sup>+</sup> and PSS<sup>-</sup>, resulting in the release of more active PEDOT<sup>+</sup>. This process improves the frictional contact area, reduces the potential barrier of the Schottky contact, and enhances the absorption of friction energy, thereby exciting more electron-hole pairs. The practical application potential of FO-TTG is demonstrated by various scenarios. The combination of six FO-TTGs in a simple series connection can successfully power electronic clocks, a thermohydrometer, and a Bluetooth wireless transmitting alarm system. Moreover, FO-TTGs, when connected in series or parallel configurations, successfully charge a mobile phone and power a small motor. These applications emphasize FO-TTG's high-output capabilities and its potential for powering a range of electronic devices. In conclusion, this work presents a record-breaking CD achieved through the combination of 95% EtOH activation in a FO-TTG. The breakthrough unveiled in this work presents vistas for the widespread application of flexible organic semiconductor textile-based TVNGs.

## MATERIALS AND METHODS

**Materials Preparation.** All experimental samples and solvents were directly used in the experiment without further purification. Poly(vinyl alcohol) (PVA) [*M<sub>w</sub>*: 98,000, Macklin], PEDOT:PSS

(P:P) [Solid particle, Net content: 1 g, Moisture content: <15%, Macklin], conductive textile (CT) [(Silver fiber, 99% pure silver layer, Antibacterial, conductive, radiation resistant), (Nylon yarn, flexibility), Aladdin], ethanol absolute [99.9% Ethanol, methanol-free, formaldehyde-free, Ester-free, unadulterated alcohol-oil-free, CAS:64-17-5, *M<sub>w</sub>*: 46.07, Macklin], and 95, 85, and 75% ethyl alcohol used in the research are mixed with ethanol absolute and DIW in a certain volume ratio, Dichloromethane (DCM) [HPLC grade, ≥ 99.9%, CAS: 75-09-2, *M<sub>w</sub>*: 84.93, Macklin], ethylene glycol (EG) [Analytical standard, ≥99.9%, CAS: 107-21-1, *M<sub>w</sub>*: 62.07, Macklin], dimethyl sulfoxide (DMSO) [HPLC grade, ≥99.9%, CAS: 67-68-5, *M<sub>w</sub>*: 78.13, Macklin], deionized water (DIW) [Conductivity <0.1 μS/cm in 25 °C, Specific resistance ≥18 MΩ·cm], and all solvents and materials used in this research were purchased from CAS MART.

**Preparation of FO-TTG.** The acrylic block was laser-cut to sample of dimensions 2.5 cm × 2.5 cm and 2.5 cm × 10 cm, respectively. The conductive textile was also cut to a sample of 2.5 cm × 10 cm and subsequently cleaned using DIW, EtOH, and acetone ultrasonically for 15 min, respectively. Next, 0.32 g of PVA and 5 mL of DIW were weighed and added to a 10 mL screw cap bottle. The mixture was stirred at 60 °C until a clear, homogeneous solution was obtained. Similarly, 0.02 g of P:P particles were weighed and added to a 20 mL screw cap bottle along with 10 mL of DIW. The mixture was stirred magnetically until a homogeneous solution was achieved.

In the next step, 5 mL of the PVA aqueous solution and 2 mL of the P:P aqueous solution were mixed and stirred for 15 min. To minimize the presence of bubbles, 50 μL of absolute ethanol was added to the mixed solution. The surface of the conductive textile was first coated with a layer of conductive ink to reduce the surface energy. This was achieved by heating at 120 °C, ensuring that the BF adhered tightly and securely to the conductive textile surface. The mixed solution, free from bubbles, was uniformly dispersed on the conductive ink-coated surface. The film was then heated at 40 °C until it was fully cured.

Finally, metal Al tape was completely wrapped around the surface of the acrylic blocks (2.5 cm × 2.5 cm) and then cut to a 2 cm × 2 cm, creating as a slider. The wires were connected between the Al slider and the conductive ink, with care taken to form a good ohmic contact between the conductive ink and the wires.

**Physical Characterization.** The microscopic surface morphology was characterized by using a Nova Nano SEM 450, which is a scanning electron microscope (SEM) imaging system manufactured in the Czech Republic. Stress-strain curve was conducted by E3000 (Instron Corporation). A Keithley 2410 Source Meter was characterized by the *I*-*V* curve of interface between BF, P:P film, and metal Al. Four-probe resistance tester (BEST-300C) was used to measure the surface conductivity of BF, P:P film, and PVA film. A Keithley 6517B Electrometer or 6514 Electrometer was used to measure the output performance of real-time open-circuit voltage (*V*<sub>OC</sub>) and short-circuit current (*I*<sub>SC</sub>) of FO-TTG. An automatic contact angle measuring instrument (CAPST-2000At, China) was used to characterize the contact angle of conductive ink layer and BF. VERTEX80v (Germany) was used to characterize the infrared absorption spectrum of different films. The X-ray diffraction (XRD) characterization of the film was processed by X'Pert3 Powder (Netherlands). Thermogravimetric analysis (TGA) and derivative thermogravimetry analysis (DTGA) were characterized by Mettler (Switzerland).

## ASSOCIATED CONTENT

### Data Availability Statement

All data generated and analyzed are included in the paper and its Supporting Information. All custom codes or algorithms used to generate results that are reported in this manuscript are available from the corresponding authors upon reasonable request.

**SI Supporting Information**

The Supporting Information is available free of charge at <https://pubs.acs.org/doi/10.1021/acsnano.4c11010>.

Physical characterization and isothermal–isobaric molecular dynamics (NVT-MD) simulation for different solvent system (PDF)

Comparison of LED driven directly by 6 FO-TTGs in series and 3 V lithium coin cell, respectively (Movie S1) (MP4)

6 Series-connected FO-TTGs simultaneously drive 6 electronic clocks in parallel (Movie S2) (MP4)

6 Series-connected FO-TTGs charge a 1 mF capacitor, and then drive the thermohydrometer (Movie S3) (MP4)

6 Series-connected FO-TTG-driven Bluetooth wireless transmitting alarm system (Movie S4) (MP4)

6 FO-TTGs in series charge for a mobile phone (Movie S5) (MP4)

6 Parallel-connected FO-TTGs first charge a 2 F capacitor, then drive a motor (Movie S6) (MP4)

**AUTHOR INFORMATION****Corresponding Author**

**Chi Zhang** – CAS Center for Excellence in Nanoscience, Beijing Key Laboratory of Micro-Nano Energy and Sensor, Beijing Institute of Nanoenergy and Nanosystems, Chinese Academy of Sciences, Beijing 101400, P. R. China; School of Nanoscience and Technology, University of Chinese Academy of Sciences, Beijing 100049, P. R. China; Center on Nanoenergy Research, School of Physical Science and Technology, Guangxi University, Nanning 530004, P. R. China; [orcid.org/0000-0002-7511-805X](https://orcid.org/0000-0002-7511-805X); Email: [czhang@binn.cas.cn](mailto:czhang@binn.cas.cn)

**Authors**

**Guoxu Liu** – CAS Center for Excellence in Nanoscience, Beijing Key Laboratory of Micro-Nano Energy and Sensor, Beijing Institute of Nanoenergy and Nanosystems, Chinese Academy of Sciences, Beijing 101400, P. R. China; School of Nanoscience and Technology, University of Chinese Academy of Sciences, Beijing 100049, P. R. China

**Beibei Fan** – Center on Nanoenergy Research, School of Physical Science and Technology, Guangxi University, Nanning 530004, P. R. China

**Youchao Qi** – CAS Center for Excellence in Nanoscience, Beijing Key Laboratory of Micro-Nano Energy and Sensor, Beijing Institute of Nanoenergy and Nanosystems, Chinese Academy of Sciences, Beijing 101400, P. R. China; School of Nanoscience and Technology, University of Chinese Academy of Sciences, Beijing 100049, P. R. China

**Kai Han** – CAS Center for Excellence in Nanoscience, Beijing Key Laboratory of Micro-Nano Energy and Sensor, Beijing Institute of Nanoenergy and Nanosystems, Chinese Academy of Sciences, Beijing 101400, P. R. China; School of Nanoscience and Technology, University of Chinese Academy of Sciences, Beijing 100049, P. R. China; [orcid.org/0000-0002-1345-3207](https://orcid.org/0000-0002-1345-3207)

**Jie Cao** – CAS Center for Excellence in Nanoscience, Beijing Key Laboratory of Micro-Nano Energy and Sensor, Beijing Institute of Nanoenergy and Nanosystems, Chinese Academy of Sciences, Beijing 101400, P. R. China; Institute of Intelligent Flexible Mechatronics, Jiangsu University, Zhenjiang 212013, P. R. China

**Xianpeng Fu** – CAS Center for Excellence in Nanoscience, Beijing Key Laboratory of Micro-Nano Energy and Sensor, Beijing Institute of Nanoenergy and Nanosystems, Chinese Academy of Sciences, Beijing 101400, P. R. China; School of Nanoscience and Technology, University of Chinese Academy of Sciences, Beijing 100049, P. R. China

**Zhaozheng Wang** – CAS Center for Excellence in Nanoscience, Beijing Key Laboratory of Micro-Nano Energy and Sensor, Beijing Institute of Nanoenergy and Nanosystems, Chinese Academy of Sciences, Beijing 101400, P. R. China; School of Nanoscience and Technology, University of Chinese Academy of Sciences, Beijing 100049, P. R. China

**Tianzhao Bu** – CAS Center for Excellence in Nanoscience, Beijing Key Laboratory of Micro-Nano Energy and Sensor, Beijing Institute of Nanoenergy and Nanosystems, Chinese Academy of Sciences, Beijing 101400, P. R. China; School of Nanoscience and Technology, University of Chinese Academy of Sciences, Beijing 100049, P. R. China; [orcid.org/0000-0003-1295-7080](https://orcid.org/0000-0003-1295-7080)

**Jianhua Zeng** – Center on Nanoenergy Research, School of Physical Science and Technology, Guangxi University, Nanning 530004, P. R. China

**Sicheng Dong** – CAS Center for Excellence in Nanoscience, Beijing Key Laboratory of Micro-Nano Energy and Sensor, Beijing Institute of Nanoenergy and Nanosystems, Chinese Academy of Sciences, Beijing 101400, P. R. China; School of Nanoscience and Technology, University of Chinese Academy of Sciences, Beijing 100049, P. R. China

**Likun Gong** – CAS Center for Excellence in Nanoscience, Beijing Key Laboratory of Micro-Nano Energy and Sensor, Beijing Institute of Nanoenergy and Nanosystems, Chinese Academy of Sciences, Beijing 101400, P. R. China; School of Nanoscience and Technology, University of Chinese Academy of Sciences, Beijing 100049, P. R. China

**Zhong Lin Wang** – CAS Center for Excellence in Nanoscience, Beijing Key Laboratory of Micro-Nano Energy and Sensor, Beijing Institute of Nanoenergy and Nanosystems, Chinese Academy of Sciences, Beijing 101400, P. R. China; School of Nanoscience and Technology, University of Chinese Academy of Sciences, Beijing 100049, P. R. China

Complete contact information is available at: <https://pubs.acs.org/doi/10.1021/acsnano.4c11010>

**Author Contributions**

All of the authors contributed to the manuscript. Conceptualization: G.X.L. Methodology: G.X.L., B.B.F., Y.C.Q. Investigation: G.X.L., Z.Z.W., J.H.Z. Visualization: G.X.L., K.H. Supervision: S.C.D., J.C., C.Z. Writing—original draft: G.X.L. Writing—review and editing: G.X.L., C.Z., Z.L.W. Software: T.Z.B., L.K.G. Editing: X.P.F.

**Notes**

The authors declare no competing financial interest.

**ACKNOWLEDGMENTS**

This research was supported by the National Natural Science Foundation of China (52450006, U23A20640) and Beijing Natural Science Foundation (L247020).

**REFERENCES**

- (1) Liu, Y. M.; Yiu, C. K.; Song, Z.; Huang, Y.; Yao, K. M.; Wong, T.; Zhou, J. K.; Zhao, L.; Huang, X. C.; Nejad, S. K.; Wu, M. G.; Li, D. F.; He, J. H.; Guo, X.; Yu, J. S.; Feng, X.; Xie, Z. Q.; Yu, X.

Electronic Skin As Wireless Human–Machine Interfaces for Robotic VR. *Sci. Adv.* **2022**, *8* (2), No. eabl6700.

(2) Zhao, Y. C.; Wang, B.; Hojaiji, H.; Wang, Z. Q.; Lin, S. Y.; Yeung, C.; Lin, H. S.; Mgyuen, P.; Chiu, K. L.; Salah, K.; Cheng, X. B.; Tan, J. W.; Cerrillos, B. A.; Emaminejad, S. A Wearable Freestanding Electrochemical Sensing System. *Sci. Adv.* **2020**, *6* (12), No. eaaz0007.

(3) Liu, G. X.; Gao, Y. Y.; Xu, S. H.; Bu, T. Z.; Xie, Y. Y.; Xu, C. Q.; Zhou, H.; Qi, Y. C.; Zhang, C. One-Stop Fabrication of Triboelectric Nanogenerator Based on 3D Printing. *EcoMat* **2021**, *3* (5), No. e12130.

(4) Xu, F.; Dong, S.; Liu, G. X.; Pan, C. X.; Guo, Z. H.; Guo, W. L.; Li, L. W.; Liu, Y. P.; Zhang, C.; Pu, X.; Wang, Z. L. Scalable Fabrication of Stretchable and Washable Textile Triboelectric Nanogenerators as Constant Power Sources for Wearable Electronics. *Nano Energy* **2021**, *88*, No. 106247.

(5) Zheng, Q.; Shi, B.; Fan, F. R.; Wang, X. X.; Yan, L.; Yuan, W. W.; Wang, S. H.; Liu, H.; Li, Z.; Wang, Z. L. In Vivo Powering of Pacemaker by Breathing-Driven Implanted Triboelectric Nanogenerator. *Adv. Mater.* **2014**, *26* (33), 5851–5856.

(6) Wang, Z. L. Triboelectric Nanogenerator (TENG)—Sparking an Energy and Sensor Revolution. *Adv. Energy Mater.* **2020**, *10* (17), No. 2000137.

(7) Wang, Z. L. On the First Principle Theory of Nanogenerators From Maxwell's Equations. *Nano Energy* **2020**, *68*, No. 104272.

(8) Zhou, H.; Liu, G. X.; Zeng, J. H.; et al. Recent Progress of Switching Power Management for Triboelectric Nanogenerators. *Sensors* **2022**, *22* (4), 1668.

(9) Wen, F.; Zhang, Z. X.; He, T. Y. Y.; Lee, C. K. AI Enabled Sign Language Recognition and VR Space Bidirectional Communication Using Triboelectric Smart Glove. *Nat. Commun.* **2021**, *12* (1), No. 5378.

(10) Parida, K.; Thangavel, G.; Cai, G. F.; Zhou, X. R.; Park, S.; Xiong, J. Q.; Lee, P. S. Extremely Stretchable and Self-Healing Conductor Based on Thermoplastic Elastomer for All-Three-Dimensional Printed Triboelectric Nanogenerator. *Nat. Commun.* **2019**, *10* (1), No. 2158.

(11) Liang, X.; Jiang, T.; Liu, G. X.; Xiao, T. X.; Xu, L.; Li, W.; Xi, F. B.; Zhang, C.; Wang, Z. L. Triboelectric Nanogenerator Networks Integrated With Power Management Module for Water Wave Energy Harvesting. *Adv. Funct. Mater.* **2019**, *29* (41), No. 1807241.

(12) Liang, X.; Jiang, T.; Liu, G. X.; Feng, Y. W.; Zhang, C.; Wang, Z. L. Spherical Triboelectric Nanogenerator Integrated with Power Management Module for Harvesting Multidirectional Water Wave Energy. *Energy Environ. Sci.* **2020**, *13* (1), 277–285.

(13) He, T.; Wang, H.; Wang, J.; Tian, X.; Lee, C. K.; et al. Self-Sustainable Wearable Textile Nano-Energy Nano-System (NENS) for Next-Generation Healthcare Applications. *Adv. Sci.* **2019**, *6* (24), No. 1901437.

(14) Hao, Y.; Wen, J.; Gao, X.; Nan, D.; Pan, J.; Yang, Y.; Chen, B. D.; Wang, Z. L. Self-Rebound Cambered Triboelectric Nanogenerator Array for Self-Powered Sensing in Kinematic Analytics. *ACS Nano* **2022**, *16* (1), 1271–1279.

(15) Cheng, B. L.; Ma, J. X.; Li, G. D.; Bai, S.; Xu, Q.; Cui, X.; Cheng, L.; Qin, Y.; Wang, Z. L. Mechanically Asymmetrical Triboelectric Nanogenerator for Self-Powered Monitoring of In Vivo Microscale Weak Movement. *Adv. Energy Mater.* **2020**, *10* (27), No. 2000827.

(16) Chen, C.; Chen, L.; Wu, Z.; Guo, H.; Yu, W.; Du, Z.; Wang, Z. L. 3D Double-Faced Interlock Fabric Triboelectric Nanogenerator for Biomotion Energy Harvesting and As Self-Powered Stretching and 3D Tactile Sensors. *Mater. Today* **2020**, *32*, 84–93.

(17) Wu, H.; Wang, S.; Wang, Z. K.; Zi, Y. L. Achieving Ultrahigh Instantaneous Power Density of 10 MW/m<sup>2</sup> by Leveraging the Opposite-charge Enhanced Transistor-like Triboelectric Nanogenerator (OCT-TENG). *Nat. Commun.* **2021**, *12* (1), No. 5470.

(18) Zhang, Z.; Gong, L. K.; Luan, R. F.; Feng, Y.; Cao, J.; Zhang, C. Tribovoltaic Effect: Origin, Interface, Characteristic, Mechanism & Application. *Adv. Sci.* **2024**, *11* (15), No. 2305460.

(19) Bhattacharya, D.; Mukherjee, S.; Chowdhury, A.; Ray, S. K. Novel TMDC/Si Heterojunction Based Direct Current UV Sensitive Tribovoltaic Nanogenerator and Visual-Image Sensors. *Adv. Funct. Mater.* **2024**, *34* (40), No. 2403705.

(20) Dong, S. C.; Bu, T. Z.; Wang, Z. Z.; Feng, Y.; Liu, G. X.; Zeng, J. H.; Wang, Z. H.; Cao, J.; Zhang, Z.; Liu, F.; Zhang, C. Freestanding-Mode Tribovoltaic Nanogenerator for Harvesting Sliding and Rotational Mechanical Energy. *Adv. Energy Mater.* **2023**, *13* (16), No. 2300079.

(21) Wang, Z. L.; Wang, A. C. On The Origin of Contact-Electrification. *Mater. Today* **2019**, *30*, 34–51.

(22) Lin, S. Q.; Wang, Z. L. The Tribovoltaic Effect. *Mater. Today* **2023**, *62*, 111–128.

(23) Shao, H.; Fang, J.; Wang, H.; et al. Schottky Direct-Current Energy Harvesters with Large Current Output Density. *Nano Energy* **2019**, *62*, 171–180.

(24) Zhang, Z.; Wang, Z. Z.; Chen, Y. K.; Feng, Y.; Dong, S. C.; Zhou, H.; Wang, Z. L.; Zhang, C. Semiconductor Contact-Electrification-Dominated Tribovoltaic Effect for Ultrahigh Power Generation. *Adv. Mater.* **2022**, *34* (20), No. e2200146.

(25) Lin, S. S.; Lu, Y. H.; Feng, S. R.; Hao, Z. Z.; Yan, Y. F. A High Current Density Direct-Current Generator Based on a Moving Van Der Waals Schottky Diode. *Adv. Mater.* **2019**, *31* (7), No. 1804398.

(26) Shao, H.; Fang, J.; Wang, H.; et al. Doping Effect on Conducting Polymer-Metal Schottky DC Generators. *Adv. Electron. Mater.* **2019**, *5* (2), No. 1800675.

(27) Meng, J.; Guo, Z. H.; Pan, C. X.; Wang, L. Y.; Chang, C. Y.; Li, L. W.; Pu, X.; Wang, Z. L. Flexible Textile Direct-Current Generator Based on the Tribovoltaic Effect at Dynamic Metal-Semiconducting Polymer Interfaces. *ACS Energy Lett.* **2021**, *6* (7), 2442–2450.

(28) Yang, R. Z.; Benner, M.; Guo, Z. P.; Zhou, C.; Liu, J. High-Performance Flexible Schottky DC Generator Via Metal/Conducting Polymer Sliding Contacts. *Adv. Funct. Mater.* **2021**, *31* (43), No. 2103132.

(29) Xu, C.; Yu, J. R.; Huo, Z. W.; Wang, Y. F.; Sun, Q. J.; Wang, Z. L. Pursuing the Tribovoltaic Effect for Direct-current Triboelectric Nanogenerators. *Energy Environ. Sci.* **2023**, *16*, 983–1006.

(30) You, Z. Y.; Wang, S. T.; Li, Z. Z.; Zou, Y. X.; Lu, T. Y.; Wang, F.; Hu, B. X.; Wang, X.; Li, L.; Fang, W. H.; Liu, Y. High Current Output Direct-Current Triboelectric Nanogenerator Based on Organic Semiconductor Heterojunction. *Nano Energy* **2022**, *91*, No. 106667.

(31) Shao, H.; Fang, J.; Wang, H. X.; Zhou, H.; Lin, T. Direct Current Energy Generators From a Conducting Polymer–Inorganic Oxide Junction. *J. Mater. Chem. A* **2017**, *5*, 8267–8273.

(32) Lin, T.; Shao, H.; Fang, J. Conducting Polymer-Based DC Generators. *Vid. Proc. Adv. Mater.* **2021**, *2* (2), No. 2102131, DOI: 10.5185/vpoam.2021.02131.

(33) Liu, G. X.; Luan, R. F.; Qi, Y. C.; Gong, L. K.; Cao, J.; Wang, Z. Z.; Liu, F.; Zeng, J.; Huang, X. L.; Qin, Y. H.; Dong, S. C.; Feng, Y.; Huang, L.-B.; Zhang, C. Organic Tribovoltaic Nanogenerator with Electrically and Mechanically Tuned Flexible Semiconductor Textile. *Nano Energy* **2023**, *106* (1), No. 108075.

(34) Campos, M.; Simoes, F. R.; Pereira, E. C. Influence of Methane in the Electrical Properties of Polypyrrole Films Doped with Dodecylbenzene Sulfonic Acid. *Sens. Actuators, B* **2007**, *125* (1), 158–166.

(35) Janardhanam, V.; Yun, H. J.; Jyothi, I.; Lee, J.; Hong, H.; Reddy, V. R.; Choi, C.-J. Energy-Level Alignment and Electrical Properties of Al/p-type Si Schottky Diodes with Sorbitol-Doped PEDOT:PSS as an Organic Interlayer. *J. Alloys Compd.* **2015**, *637*, 84–89.

(36) Ouyang, J. Y.; Xu, Q. F.; Chu, C. W.; Yang, Y.; Li, G.; Shinar, J. On the Mechanism of Conductivity Enhancement in Poly(3,4-ethylenedioxythiophene):poly(styrene sulfonate) Film through Solvent Treatment. *Polymer* **2004**, *45* (25), 8443–8450.

(37) Bai, Y.; Meng, H. Y.; Li, Z.; Wang, Z. L. Degradable Piezoelectric Biomaterials for Medical Applications. *MedMat* **2024**, *1* (1), 40–49.

(38) Gao, Y.; Li, H.; Chao, S. Y.; Wang, Y. Q.; Hou, L. L.; Bai, T. H.; Bai, J.; Man, X. K.; Cui, Z. M.; Wang, N.; Li, Z.; Zhao, Y. Zebra-Patterned Stretchable Helical Yarn for Triboelectric Self-Powered Multifunctional Sensing. *ACS Nano* **2024**, *18* (26), 16958–16966.

(39) Liu, Y.; Wang, C.; Liu, Z.; Qu, X. S.; Gai, Y. S.; Xue, J. T.; Chao, S. Y.; Huang, J.; Wu, Y. X.; Li, Y. S.; Luo, D.; Li, Z. Self-Encapsulated Ionic Fibers Based on Stress-Induced Adaptive Phase Transition for Non-Contact Depth-of-Field Camouflage Sensing. *Nat. Commun.* **2024**, *15* (1), No. 663.

(40) Meng, H. Y.; Yu, Q.; Liu, Z.; Gai, Y. S.; Xue, J. T.; Bai, Y.; Qu, X. C.; Tan, P. C.; Luo, D.; Huang, W. W.; Nie, K. X.; Bai, W.; Hou, Z. S.; Tang, R. P.; Xu, H. X.; Zhang, Y.; Cai, Q.; Yang, X. Z.; Wang, Z. L.; Li, Z. Triboelectric Performances of Biodegradable Polymers. *Matter* **2023**, *6* (12), 4274–4290.

(41) He, H.; Ouyang, J. Y. Enhancements in the Mechanical Stretchability and Thermoelectric Properties of PEDOT:PSS for Flexible Electronics Applications. *Acc. Mater. Res.* **2020**, *1* (2), 146–157.